ORIGINAL CONTRIBUTION

FFEMS Fatigue & Fracture of Engineering Materials & Structures WILEY

# Fatigue assessment of as-built and heat-treated Inconel 718 specimens produced by additive manufacturing including notch effects

Klas Solberg | Di Wan | Filippo Berto

Department of Mechanical and Industrial Engineering, Norwegian University of Science and Technology, Trondheim, Norway

**Correspondence**
Klas Solberg, Department of Mechanical and Industrial Engineering, Norwegian University of Science and Technology, 7034 Trondheim, Norway.
Email: klas.solberg@ntnu.no

## Abstract

The fatigue behaviour of notched and unnotched specimens produced by additively manufactured Inconel 718 were analysed in the as-built and heat-treated conditions. The surfaces display high roughness and defects acting as fatigue initiation sites. In the as-built condition, fine subgrains were found, while in in the heat-treated state, the subgrains were removed and the dislocation density recovered. SN-curves are predicted based on tensile properties, hardness and defects obtained by fractography, using the $\sqrt{\text{area}}$-method.

## KEYWORDS

additive materials, fatigue, heat treatment, Inconel 718, selective laser melting, small defects

## 1 | INTRODUCTION

Additive manufacturing (AM) is a fast-rising production method allowing components to be produced by adding material rather than forming or subtracting, as is characteristic for many established conventional processes. Many design restrictions are avoided with AM, and parts can be manufactured with a high degree of design freedom. However, some challenges also arise with the new manufacturing method: high surface roughness, anisotropic microstructure, porosity and residual stresses.[1-5] Due to this, the fatigue behaviour of the materials are often reduced compared with the wrought condition.[6] In particular, the geometric defects such as porosity, surface roughness and lack of fusion reduce the fatigue strengths.[6-10] The defects in the surface region can be removed by machining, and internal pores can be closed by hot isostatic pressing. In many cases, machining is not possible due to the desired complexity of the designed components. However, heat treatments might still be possible to improve the fatigue performance. This is particularly true for alloys such as

Inconel 718, whose performance is strongly correlated to the heat treatment schemes.

Inconel 718 is a precipitation hardening alloy that displays high yield, tensile, creep and fatigue strengths at temperatures up to 700°C. In addition to this, the alloy has high weldability, making it a good candidate for AM. The alloy is commonly used in the aerospace industry, and the oil and gas industry, employing different heat treatment schemes for various applications.[11] There are several possible heat treatment schemes for Inconel 718, and they usually consist of two main stages: (a) homogenization and/or solution treatment at 980°C to 1200°C for dissolving hardening constituents into the matrix and (b) ageing treatment at 650°C to 900°C for forming $\gamma'$ and $\gamma''$ precipitates. The ageing process is usually done in two steps.

Due to the high-temperature gradients in AM processes such as selective laser melting (SLM), the microstructure usually shows different features than those produced by conventional manufacturing.[12] Typically fine subgrain/dendritic structures are observed in the as-built

(AB) state.[13] As a result of this, researchers are working on tailoring heat treatments for AM applications.[13,14]

Dealing with fatigue, the general conclusion is that the AM Inconel 718 is sensitive to the defects deriving from the manufacturing process. The material displays its lowest fatigue strength in the AB condition, where the surface roughness tends to be high.[15] When machined, the fatigue strength of the material is increased.[15] Here, defects may be present as internal porosity or lack-of-fusion. Their locations and distributions usually cause a higher scatter in the fatigue data.[15] In terms of anisotropy, the specimens manufactured horizontally display longer fatigue life than those manufactured vertically.[1,16,17] Hot isostatic pressing (HIP) can close internal porosity and has been reported to increase the fatigue strength to the same level as wrought[18]; however, it has also been reported to reduce the strength due to microstructural effects.[19]

Dealing with the influence of notches on the fatigue behaviour of AM Inconel 718, several different approaches have been made. By machining and HIPing the specimens, the designed notch can be taken into account without the influence of defects deriving from the manufacturing process.[20] If the specimens are tested in the AB condition (or if internal defects are present after machining), the surface defects also act as local notches within the notch geometries.[20-23] Taking advantage of the design freedom in AM, parts are likely to contain notched regions and in addition manufacturing defects. Due to this, it is important to address issues related to size effects, both for determining the critical size and location of the defects[24,25] and for determining the appropriate dimensions of testing specimens[22,23]

In this work, the fatigue behaviour of AM Inconel 718 are investigated in the AB and the heat-treated (HT) states. This was done for both notched and unnotched specimens. The microstructures of the two different material states were investigated and compared. Defects from the fracture surfaces were captured, and the hardness of the two materials were measured. SN-curves of the different materials and geometries were predicted based on the tensile properties and the $\sqrt{area}$-method[26] using hardness and defect sizes.

It should be noted that this work is a continuation of a previous work where the fatigue behaviour was studied in the AB condition,[22] and the same specimen geometries and process parameters have been used.

## 2 | MATERIALS AND METHODS

In the present work, Inconel 718 specimens produced by SLM are studied. The chemical composition of the material is defined in Table 1 based on ASTM F3055-14a.[27] Three different specimen geometries were considered: one specimen geometry for static loading and two specimen geometries for fatigue loading. The geometries are shown in Figure 1. The specimen for quasi-static loading was designed according to ASTM E8. The two geometries for fatigue loading were the same as the ones employed in a previous work by the authors (Solberg and Berto[22]): one unnotched and one double v-notch geometry with stress concentrations, $K_t$, of 1.07 and 2.43, respectively.[22] The specimens were manufactured layer by layer in z-direction referring to thecoordinate system in Figure 1. A layer height of 50 $\mu$m and an energy density of 60 J/mm$^3$ were employed in the SLM process.

The specimens were tested in two different conditions: AB and HT. The heat treatment was done in multiple steps; first 1 h at 1,095ºC followed by air cooling to room temperature, then double ageing, first 8 h at 720ºC followed by furnace cooling at 50°C/h until 620ºC and aged for 8 h. Finally the specimens were air cooled to room temperature.

Mechanical loading was done using a servohydraulic MTS uniaxial testing system with a load cell of 50 kN. The fatigue testing was done using the same system, a loading ratio $R = 0$ and a frequency of 10 Hz were used. Vickers hardness measurements were done on a Mitutoyo MicroWiZhard system; the reported values were taken as the average and standard deviation of 10 measurements in each orientation.

Fractography was done using a Quanta FEG 650 scanning electron microscope (SEM). The microstructure was analysed by different approaches. Analysis done by optical microscope was done by polishing cross-sections and Kalling's reagent according to ASTM E407-07. The final stage of polishing was 1-$\mu$m diamond paste. For electron backscatter diffraction (EBSD) and backscattered-electron (BSE) analysis, the specimens were not etched but prepared by oxide polishing suspensions, with a particle size of 0.25 $\mu$m.

## 3 | RESULTS

### 3.1 | Mechanical behaviour and fatigue data

Based on the tensile tests, the AB specimen showed a tensile strength of 948 MPa and an elongation of 13.0%. After HT, a tensile strength of 1,374 MPa and an elongation of 7.7% were achieved. The increase in strength and reduction in elongation at failure are typical when heat-treating AM Inconel 718.[1,28] However, the results obtained here show somewhat lower elongation the other
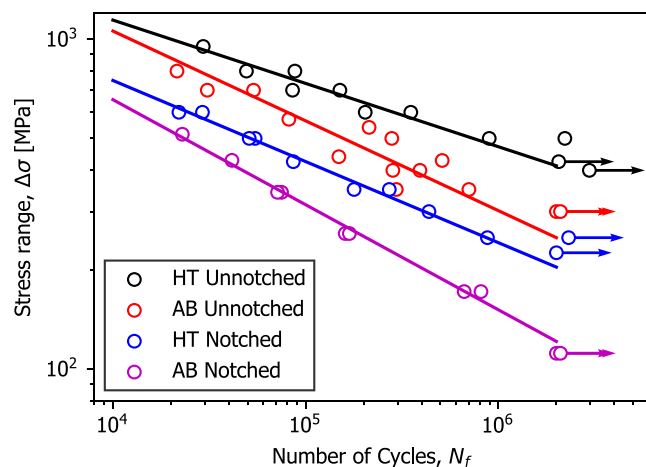
**TABLE 1** Chemical composition of Inconel 718 as defined by ASTM F3055-14a in wt%[27]

| Ni | Fe | Cr | Nb | Mo | Ti | Al | Co | Si | Mn | Cu |
|---|---|---|---|---|---|---|---|---|---|---|
| 50-55 | 11-22.4 | 17-21 | 4.8-5.5 | 2.8-3.3 | 0.7-1.2 | 0.2-0.8 | 1.0 | 0.4 | 0.4 | 0.3 |
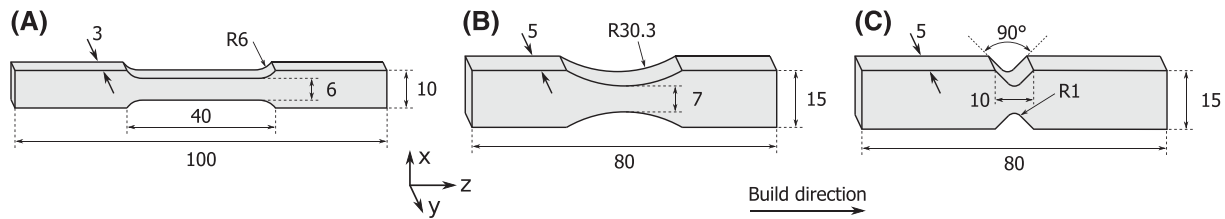


**FIGURE 1** Dimensions of specimens: (A) tensile specimen, thickness 3 mm; (b) unnotched fatigue specimen, thickness 5 mm; and (C) notched fatigue specimens, thickness 5 mm. All specimens are built in $z$-direction

**TABLE 2** Vickers hardness measurements of AB and HT specimens in $xy$- and $xz$-planes

| AB xy | AB xz | HT xy | HT xz |
|---|---|---|---|
| $314.1 \pm 16.2$ | $311.1 \pm 14.1$ | $494.5 \pm 19.0$ | $512.9 \pm 19.4$ |

Abbreviation: AB, as-built; HT, heat-treated

**TABLE 3** Summary of the fatigue strength, $\Delta\sigma$, at $2 \times 10^6$ cycles and the inverse slope, $k$, of the regression lines in Figure 2

| | $\Delta\sigma$ [MPa] | $k$ |
|---|---|---|
| HT Unnotched | 420.5 | 5.21 |
| AB Unnotched | 250.0 | 3.67 |
| HT Notched | 203.2 | 4.07 |
| AB Notched | 121.2 | 3.14 |

The fatigue data are collected in the SN-diagram in Figure 2. Both for unnotched and notched specimens, the fatigue strength is increased when comparing HT to AB. Basquin equation regression lines were added in the range of $10^4$ and $2 \times 10^6$ cycles; the fatigue strength at $2 \times 10^6$ cycles and the inverse slope of the curves are shown in Table 3.

## 3.2 | Fractographies

Fracture surfaces of the four different specimen types are shown in Figure 3A-D. In the unnotched specimens (Fig 3A,B), the same trend is observed for AB and HT: fatigue initiates from a local defect in the surface and propagates towards the other side of the specimen (indicated by the arrows). For the notched specimens (Figure 3C,D), two different fracture processes are observed: crack propagation from both notches (Figure 3C) and crack propagation from one notch(in Figure 3D). The AB specimens experienced crack propagation from both notches, while the HT specimens had both cases.

The size and morphology of the defects initiating fatigue are shown in Figure 3E-H. No distinct differences in the defect morphologies are observed when comparing the AB specimens to the HT specimens; the unnotched specimens fail from local defects, while the notched
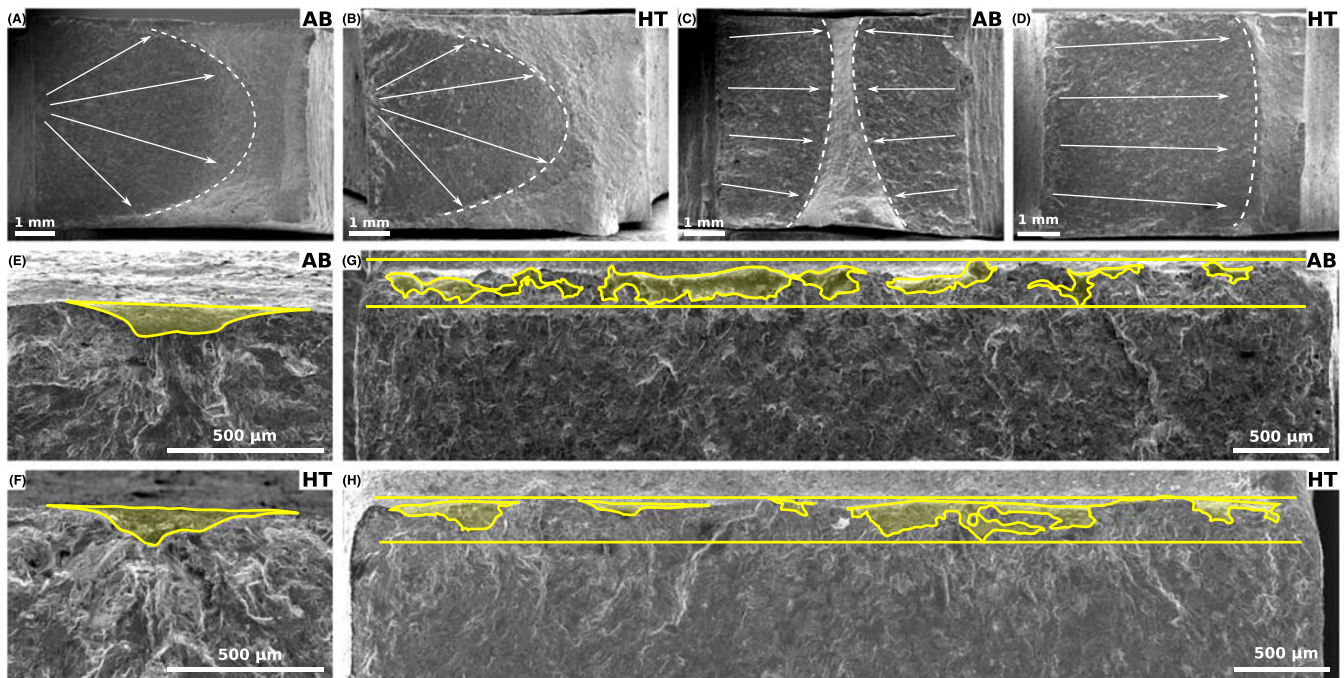


**FIGURE 2** Fatigue data of heat-treated (HT) and as-built (AB) specimens. Tests were performed with a loading ratio $R = 0$ and frequency of 10 Hz [Colour figure can be viewed at wileyonlinelibrary.com]

data in the literature.[1] The low elongation in both cases can be attributed to the fact that the specimens were tested with the AB surface. A strong correlation between the surface roughness and elongation at failure for Ti6Al4V was recently demonstrated by Barba et al.[29]

Hardness measurements of the AB and HT materials were done in the $xy$- and $xz$-planes, referring to the coordinate system in Figure 1. The results are shown in Table 2 and shows that for AB, the hardness was approximately 300 HV, and for HT, the hardness was approximately 500 HV.

**FIGURE 3** Fracture surface and detail of defects initiating fatigue of the different specimen types: (A and B) unnotched, overview; (C and D) notched, overview; (E and F) unnotched, initiation; and (G and H) notched, initiation. The material conditions are indicated in each subfigure [Colour figure can be viewed at wileyonlinelibrary.com]

specimens fail from defects distributed along the thickness direction of the sample.

## 3.3 | Failure locations and surface defects

The cross-sections of one AB and one HT notched specimen subjected to $2\times10^6$ cycles of loading are compared in Figure 4A,B. The same general trends are observed: defect populated down-skin region and smoother up-skin surface. The AB specimen displays fatigue crack initiation from the down-skin region; this is not observed within the HT specimen. It should be noted that the morphology of the defects adjacent to the notch root is not the same. Further, Figure 4 evaluates one plane within the material, which is not necessarily representable for the whole cross-section.

According to recent research, notch geometries produced by AM subjected to fatigue loading do not necessarily fail from the designed notches, but rather from defects related to the manufacturing process, dependent on the notch acuity and the size of the defects.[22,25] Both the AB and HT specimens display the same general surface morphology, and similar values of $Rz$ can be assumed: 77 and 259 $\mu$m for the up-skin and down-skin, respectively.[30] It should be noted that an oxide film was

formed on the surface in the HT specimens, as highlighted in Figure 4C.

The trends in failure locations are shown in Figure 4E. For the unnotched specimens, AB displays a high scatter in failure locations compared with HT. Based on these differences, it seems like the AB specimens are less sensitive to the nominal stress level and more sensitive to defects than HT. Further, some differences are observed when comparing the notched specimens. For AB specimens, fatigue initiated from both sides and always in the down-skin region. For the HT specimens, fatigue shifted between failure from one or two sides. In addition to this, some specimens failed from closer to the notch root.

## 3.4 | Microstructure

The microstructure of the AB and HT conditions are shown in Figure 5A,B, respectively. In AB, the hatch pattern and melt pool morphologies are visible, elongated grains are observed in the build direction (*xz*- and *yz*-planes) and equiaxed grains in the *xy*-plane. In the case of HT, the same general trends are observed. However, the hatching pattern and melt pool morphologies are not as visible. The general microstructure is typical for Inconel 718 produced by SLM.[1] The two materials were further analysed by EBSD, and the results are shown in Figure 6.
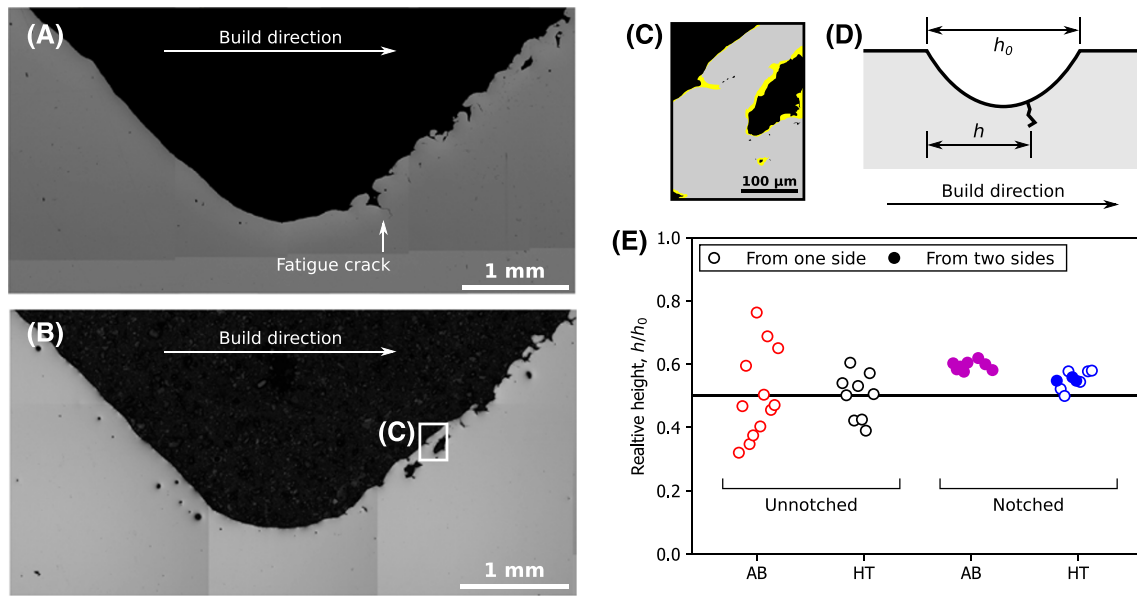
—WILEY



**FIGURE 4** Polished cross sections of notched specimens subjected to $2\times10^6$ cycles: (A) as-built (AB) and (B) heat-treated (HT). (C) Highlighted oxide layer (yellow). (D) Definition of failure site: relative height, $h/h_0$. (E) Failure locations for the various tests [Colour figure can be viewed at wileyonlinelibrary.com]
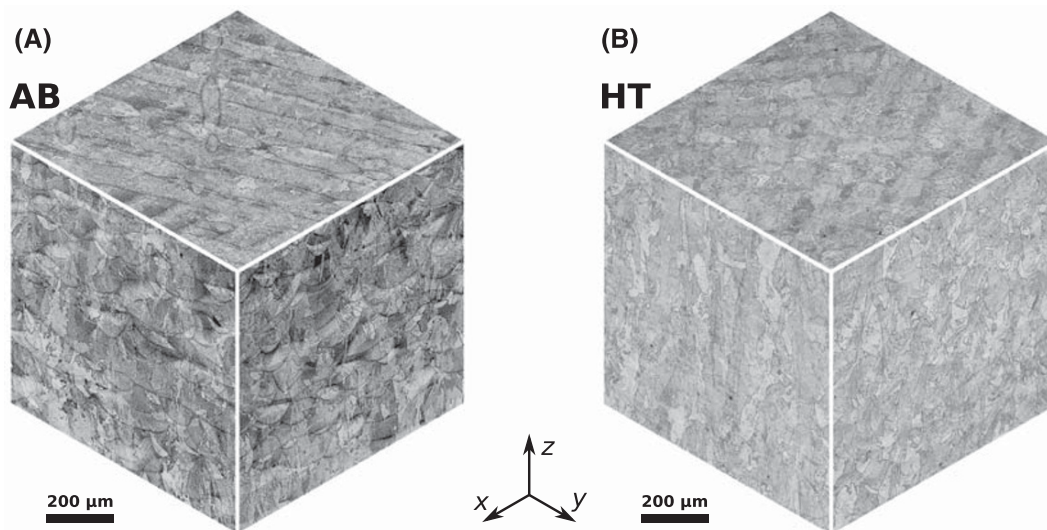


**FIGURE 5** Comparison of the general microstructure and the surface conditions in as-built (AB) and heat-treated (HT) (a) three planes of microstructure in AB and (b) three planes of microstructure in HT

The structure of the grains are shown in Figure 7. Figure 7A,D shows the difference between AB and HT in the $xz$-plane. In the AB condition, a refined subgrain structure is observed; in the HT specimen, the boundaries seem erased/smoothed compared with AB. The same trends are observed in the $xy$-plane, in Figure 7B,E. In the case of AB, the subgrains show the same trend as the general microstructure: elongated in the build direction and equiaxed in the $xy$-plane. Furthermore, precipitates are observed at the grain boundaries in the HT specimen, as indicated by arrows in Figure 7E. In addition, the

dislocation density is compared in Figure 7C,F. The white lines indicate the dislocations. Compared with AB specimens, a reduced dislocation density is observed for the HT specimens, which is the same to the results reported by Zhang et al.[28]

## 3.5 | Fatigue life predictions

When designing against fatigue, SN-diagrams are frequently used to determine the critical load levels. For
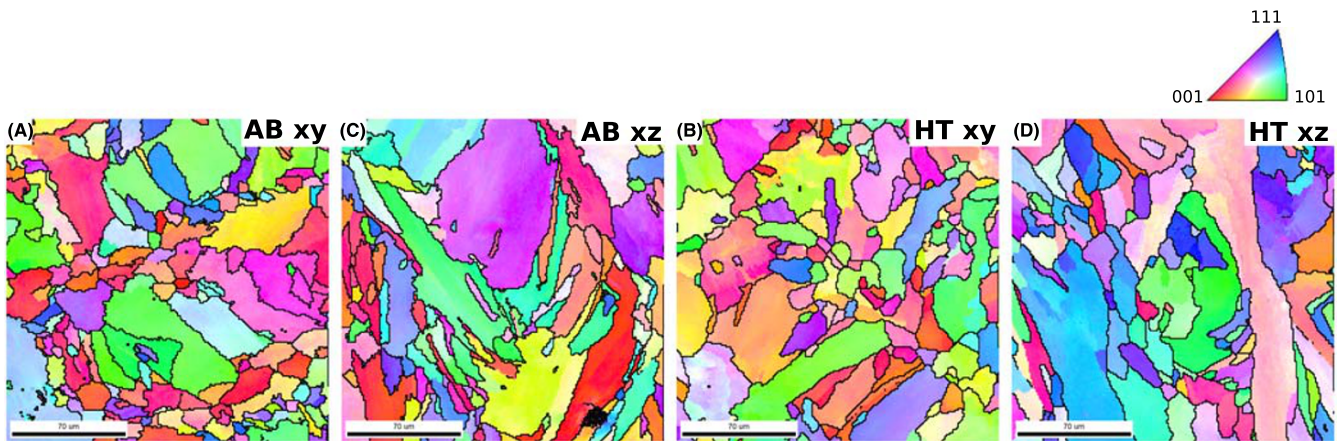
**FIGURE 6** General microstructure obtained by electron backscatter diffraction (EBSD) in terms of normal direction-inverse pole figure (ND-IPF) maps. (A) as-built (AB) *xy*-plane, (B) heat-treated (HT) *xy*-plane, (C) AB *xz*-plane and (D) HT *xz*-plane. The colouring criterion is the same for all subfigures, shown by the IPF in the upper right corner [Colour figure can be viewed at wileyonlinelibrary.com]
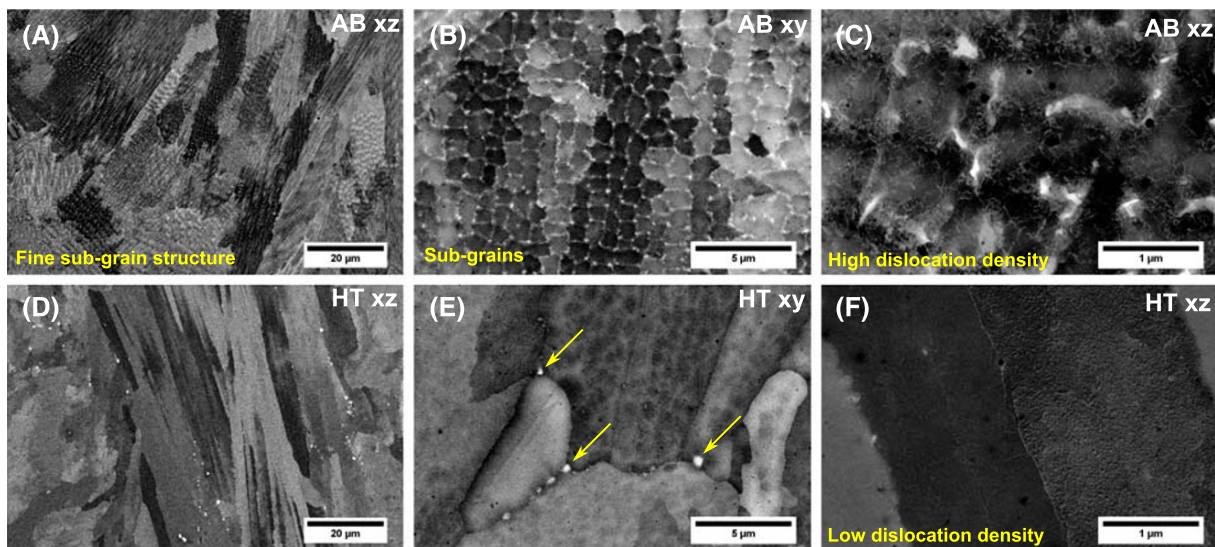


**FIGURE 7** Scanning electron microscope (SEM) analysis of the microstructure of as-built (AB) (A-C) and heat-treated (HT) (D-F) materials. (A) *xz*-plane, (B) *xy*-plane and (C) *xz*-plane, high dislocation density visible, (D) *xz*-plane, (E) *xy*-plane and (F) *xz*-plane, low dislocation density visible [Colour figure can be viewed at wileyonlinelibrary.com]

design purposes, SN-diagrams can either be developed based on experimental data or they can be estimated. In this section, we demonstrate how the Murakami method[26] and the tensile behaviour can be used for estimating SN-diagrams for AM metals.

The Murakami model has been frequently employed when analysing AM metals.[7,31-33] The model correlates the fatigue limit, $\sigma_w$, with the hardness and the critical defect size, $\sqrt{\text{area}}$. The fatigue limit can be estimated (for $R = -1$ loading) by the following relation:

$$\sigma_{w,R=-1} = \frac{1.43(Hv + 120)}{(\sqrt{\text{area}})^{1/6}}. \tag{1}$$

In order to predict the fatigue behaviour, the following assumptions were made:

1. The fatigue strength can be predicted to be equal to the tensile strength, $\sigma_{uts}$, at approximately $10^3$ cycles. This is a good estimate for many ductile engineering materials at $R = 0$.[34] This is can also be used for notched specimens due to the notch strengthening effect.[30]

2. The fatigue limit can be predicted based on the critical defect size and the hardness, employing the $\sqrt{\text{area}}$-method by Murakami. Note that the fatigue limit should also be corrected for the mean stress and the stress concentration factor.
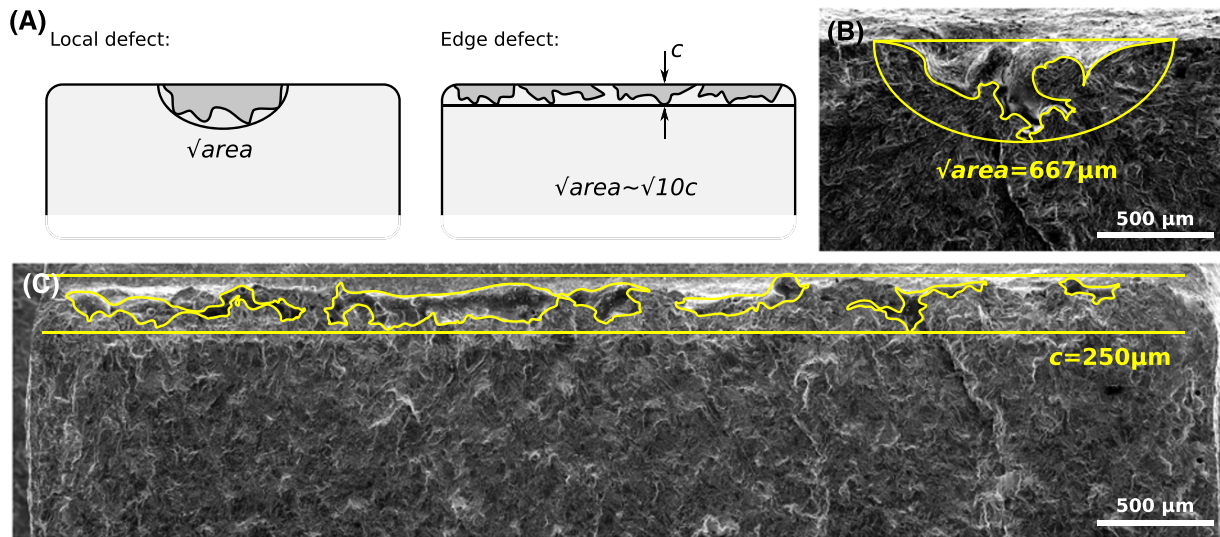
**FIGURE 8** Defects and effective defect area of (A) unnotched specimen and (B) v-notched specimen. (C) Method of estimating the effective defect area of local and edge defects [Colour figure can be viewed at wileyonlinelibrary.com]
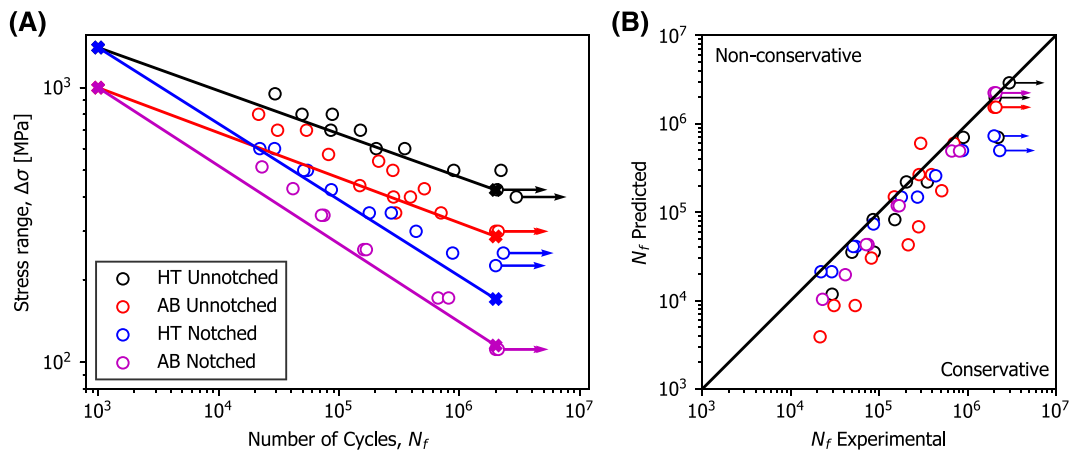


**FIGURE 9** (A) Fatigue life curves predicted based on Murakami method and tensile properties. B) Accuracy of SN-curve predictions [Colour figure can be viewed at wileyonlinelibrary.com]

3. The slope of the SN-diagram can be estimated based on the two above-mentioned estimates by the Basquin equation.

In the case of the fatigue data presented here, the defect sizes were captured for all the AB specimens. Based on the micrograph in Figure 4A,B, the surface morphologies of AB and HT specimens are similar. In addition, the fracture surfaces in Figure 3 show similar defects. This indicates that the defects obtained in the AB specimens can be used to predict the fatigue life of the HT specimens. The loading ratio for the fatigue data in this work is $R = 0$; this means that a mean stress correction should be made of the Murakami model. The SWT mean stress correction was used.[35] The SWT mean stress correction is given by

$$\sigma_{ar} = \sigma_a \sqrt{\frac{2}{1-R}}, \tag{2}$$

where $\sigma_a$ is the stress amplitude and $\sigma_{ar}$ is the equivalent stress amplitude for $R = -1$. The fatigue limit expressed in terms of the stress range corrected to $R = 0$ loading can then be expressed as

$$\Delta\sigma_{w,R=0} = \sqrt{2} \cdot \frac{1.43(Hv + 120)}{(\sqrt{\text{area}})^{1/6}}. \tag{3}$$

The $\sqrt{\text{area}}$ should be taken as the effective defect area projected onto the plane perpendicular to the loading direction. Both in the case of unnotched and notched specimens, the largest defect obtained from fractography was used. The defects and the estimated effective area are

shown in Figure 8. In the case of the unnotched specimen, a semi-ellipse was drawn around the defect. In the case of the notched specimens, defects were present along the edge of the notch, and in this case, the effective defect size was taken to be $10c$, where $c$ is the maximum depth of the defect (as suggested in by Murakami[36]). Based on these assumptions, the predicted fatigue life curves are shown in Figure 9A and the accuracy of the predictions are shown in Figure 9B.

# 4 | DISCUSSION

## 4.1 | Failure locations

In Figure 4, changes in failure locations are observed when comparing AB and HT. Several explanations can be used for describing the change in failure locations observed when comparing the AB and HT specimens.

The first explanation is based on the ideas of Wan et al, where they proposed that heat treatment of AM Inconel 718 could increase the resistance to fatigue initiating from voids.[14] It is widely accepted that the mechanical performance, and in particular the fatigue behaviour of Inconel 718, is strongly dependent on the heat treatments. By assuming that voids and defects will always be present in SLM components, Wan et al tailored heat treatments for AM Inconel 718 for making the material less sensitive to the geometric defects. This would be equivalent to altering the *critical distance* of the material.[37] The idea of the critical distance was derived from Neuber,[38,39] who proposed that failure is initiating when the stress at a certain distance (or along a structural support length) inside the material reaches a critical value.[40] That is, the stress at a certain distance away from a notch/defect/crack should reach a certain value for failure to occur. Engineering alloys with different mechanical properties have different critical distances.[37,40,41] Usually, specimens for fatigue testing are designed in order to have a fixed failure location. However, in the specimens considered here, there are several possible failure locations, that is, the local defects and the global geometry. As these two geometrical configurations (appearing at different scales) produce different stress gradients, the failure locations might shift if the critical distance of the material change. This could indicate that the shift in failure locations could be caused by a change in the critical distance after the heat treatment, making the stress field from the notch root more critical than the stress from the defects.

Another factor influencing the failure locations could be the effect of the oxide film. The oxide film in HT specimen can be observed in Figure 4C. Oxidation layers can be used as protection against corrosion.[42] The oxide film forms on free surface and might have a similar effect to what has been observed in high-temperature fatigue of Inconel 718. In high-temperature fatigue of Inconel 718, some researchers are attributing the high fatigue strength and the retardation of short crack growth to the formation of oxide films at the crack tip, which suppresses slipping.[43-47] Assuming that the AB surfaces are "precracked" due to the defects in the surface region, the initiation of crack growth might be suppressed by the oxide film. In addition to this, the oxide films could be "blunting" the defects so that an oxide layer covers their initial sharp radius. It should be noted that oxides have also been found to decrease the fatigue behaviour of materials, in particular when they take form as imperfections.[48,49] If oxide films can increase the fatigue strength in AM components, it would be a straightforward and cheap way to do postprocessing. In conventional components, the oxide film might change the appearance or the tolerances. While in AM AB components, the surfaces are initially rough, and it would not matter if an oxide film is present or not.

A third explanation could be a statistical difference in the defects of the AB and HT specimens. From Figure 4, it seems that the same morphologies of defects are present in the down-skin region for both specimens. From the fractographies in Figure 3, defects of similar sizes and morphologies were found in the AB and HT specimens.

## 4.2 | The $\sqrt{\text{area}}$-method

The modified approach of the Murakami method proposed here can give predictions of the fatigue strengths of both notched and unnotched specimens based on tensile properties, hardness and defect-size. The estimates give conservative predictions; however, this result is dependent on what number of cycles one states the fatigue limit to be at. For example, if the fatigue limit is stated to be at $10^7$ cycles, then the predictions would be less conservative. It should also be noted that many effects are not taken into account, such as residual stresses and microstructural anisotropy. Despite this, the method can be useful for estimating the fatigue properties when designing components.

One of the main issues dealing with the $\sqrt{\text{area}}$-method is that the effective defect area should be used. In order to obtain this area, specimens usually need to be broken in fatigue loading. But how much does the accuracy of the parameter matter on the fatigue limit predictions? There is a linear relationship between the hardness and the fatigue limit, while there is a power law relation between the defect size and the fatigue limit. In
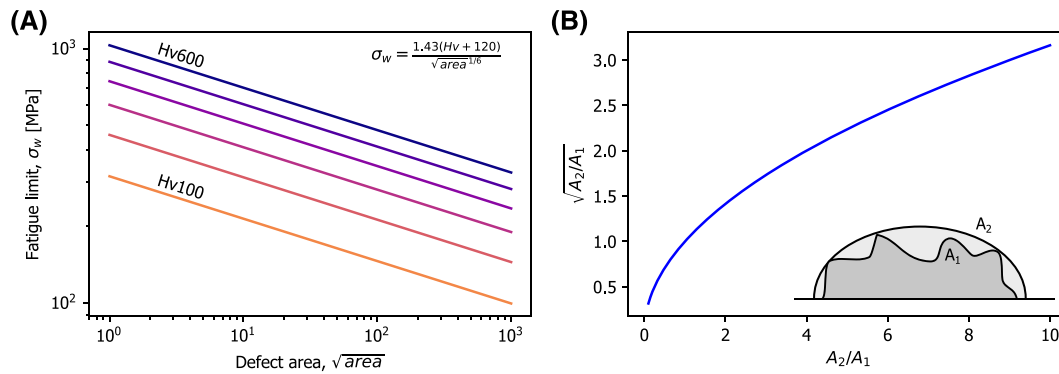
**FIGURE 10** (A) The effect of Hv and $\sqrt{area}$ on the fatigue limit predicted by Murakami. (B) The influence of the area measured [Colour figure can be viewed at wileyonlinelibrary.com]

Figure 10A, the fatigue limit predictions are plotted versus $\sqrt{area}$ for *Hv* values ranging from 100 to 600.

The measurement of the effective area in the Murakami model leaves room for deviations. The plot in Figure 10B shows the effect of deviating measurements. If $A_2$ is overestimated, for example, by a factor of 10, the resulting error in is by a factor of 0.3. This means that by taking $\sqrt{area}$, the errors are corrected to be closer to the real area.

The defect range in AM is typically one order of magnitude, for example, $10^1 - 10^2$ $\mu$m. Due to this, making a mistake in calculation, for example, 50%, will have a small impact on the result. The Murakami model is mainly concerned with the order of magnitude of the defect.

## 5 | CONCLUSIONS

AM Inconel 718 was analysed in the AB and HT states. The tensile and fatigue behaviours of the material were evaluated. Further, the Murakami model was employed for predicting SN-diagrams. The following conclusions can be drawn:

- Heat treatment of AB specimens increased the tensile strength, the hardness and the fatigue strength and decreased the elongation at failure.
- The microstructure showed typical columnar grains in the build direction for both AB and HT. In the AB state, fine subgrain structures were observed; these were erased after HT and precipitates were observed at the grain boundaries. The dislocation density was reduced after heat treatment.
- SN-curves were predicted based on the Murakami model and the tensile strengths, for both unnotched and notched specimens. The predictions indicated that the method is suitable design purposes in engineering applications.

## AUTHOR CONTRIBUTIONS

Klas Solberg: Conceptualization, Formal Analysis, Investigation, Visualization and Writing - Original Draft. Di Wan: Investigation and Writing - Review and Editing. Filippo Berto: Conceptualization, Writing - Review and Editing and Supervision.

## NOMENCLATURE

| | |
|---|---|
| $\sqrt{area}$ | *Defect size* |
| c | Maximum depth of edge defect |
| a/W | Normalized crack length ratio in L-type specimen |
| Hv | *Vickers Hardness* |
| $h_0$ | Height of notch (reduced cross section) |
| h | Failure location |
| $K_t$ | Stress concentration factor |
| $N_f$ | *Number of cycles to failure* |
| R | Loading ratio |
| $\sigma_a$ | *Stress amplitude* |
| $\sigma_{ar}$ | *Stress amplitude corrected for mean stress* |
| $\sigma_{uts}$ | *Ultimate tensile strength* |
| $\sigma_w$ | *Fatigue limit* |

## ORCID

*Klas Solberg* https://orcid.org/0000-0002-1700-6420
*Filippo Berto* https://orcid.org/0000-0001-9676-9970

## REFERENCES

1. Hosseini E, Popovich V. A review of mechanical properties of additively manufactured Inconel 718. *Addit Manuf.* 2019;30: 100877.
2. Vastola G, Zhang G, Pei Q, Zhang YW. Controlling of residual stress in additive manufacturing of Ti6Al4V by finite element modeling. *Addit Manuf.* 2016;12:231-239.

3. Megahed M, Mindt HW, N'Dri N. Duan H, Desmaison O. Metal additive-manufacturing process 288 and residual stress modeling. *Integr Mater Manuf Innov*. 2016;5:6193.

4. Salvati E, Lunt AJ, Heason CP, Baxter GJ, Korsunsky AM. An analysis of fatigue failure mechanisms in an additively manufactured and shot peened in 718 nickel superalloy. *Mater Des*. 2020;191:108605.

5. Barros R, Silva FJG, Gouveia RM, et al. Laser powder bed fusion of Inconel 718: residual stress analysis before and after heat treatment. *Metals*. 2019;12:1290.

6. Yadollahi A, Shamsaei N. N Additive manufacturing of fatigue resistant materials: challenges and opportunities. *Int J Fatigue*. 2017;98:14-31.

7. Tammas-Williams S, Withers P, Todd I, Prangnell P. The influence of porosity on fatigue crack initiation in additively manufactured titanium components. *Sci Rep*. 2017;7:7308.

8. Li P, Warner D, Fatemi A, Phan N. Critical assessment of the fatigue performance of additively manufactured Ti6Al4V and perspective for future research. *Int J Fatigue*. 2016;85:130-143.

9. Molaei R, Fatemi A, Phan N. Significance of hot isostatic pressing (HIP) on multiaxial deformation and fatigue behaviors of additive manufactured Ti-6Al-4V including build orientation and surface roughness defects. *Int J Fatigue*. 2018;7:352-370.

10. Hovig EW, Azar AS, Sunding MF, Andreassen E, Srby K. High cycle fatigue life estimation of materials processed by laser powder bed fusion. *Fatigue Fract Eng Mater Struct*. 2019;42(7):1454-1466.

11. Donachie MJ, Donachie SJ. *Superalloys, a techinal guide*: ASM International; 2002.

12. Wang Z, Guan K, Gao M, Li X, Chen X, Zeng X. The microstructure and mechanical properties of deposited IN718 by selective laser melting. *J Alloys Compd*. 2012;513:518-523.

13. Tucho WM, Cuvillier P, Sjolyst-Kverneland A, Hansen V. Microstructure and hardness studies of Inconel 718 manufactured by selective laser melting before and after solution heat treatment. *Mater Sci Eng A*. 2017;687:220-232.

14. Wan HY, Zhou ZJ, Li CP, Chen GF, Zhang GP. Enhancing fatigue strength of selective laser melting-fabricated Inconel 718 by tailoring heat treatment route. *Adv Eng Mater*. 2018;20(10):1800307.

15. Balachandramurthi AR, Moverare J, Dixit N, Pederson R. Influence of defects and as-built surface roughness on fatigue properties of additively manufactured alloy 718. *Mater Sci Eng A*. 2018;735:463-474.

16. Konecna R, Nicoletto G, Kunz L, Baa A. Microstructure and directional fatigue behavior of Inconel 718 produced by selective laser melting. *Proc Struct Integ*. 2016;2:2381-2388.

17. Kelley PF. Fatigue behavior of direct metal laser sintered (DMLS) Inconel 718. *MSc thesis*: Tufts University; 2016.

18. Witkin DB, Patel D, Albright TV, Bean GE, McLouth T. Influence of surface conditions and specimen orientation on high cycle fatigue properties of Inconel 718 prepared by laser powder bed fusion. *Int J Fatigue*. 2020;132:105392.

19. Aydinoz M, Brenne F, Schaper M, et al. On the microstructural and mechanical properties of post-treated additively manufactured Inconel 718 superalloy under quasi-static and cyclic loading. *Mater Sci Eng A*. 2016;669:246-258.

20. Witkin DB, Patel DN, Bean GE. Notched fatigue testing of Inconel 718 prepared by selective laser melting. *Fatigue Fract Eng Mater Struct*. 2019;42:166-177.

21. Nicoletto G. Smooth and notch fatigue behavior of selectively laser melted Inconel 718 with as-built surfaces. *Int J of Fatigue*. 2019;128:105211.

22. Solberg K, Berto F. Notch-defect interaction in additively manufactured Inconel 718. *Int J Fatigue*. 2019;122:35-45.

23. Konecna R, Nicoletto G, Riva E. Notch fatigue behavior of inconel 718 produced by selective laser melting. *Proc Struct Integr*. 2019;17:138-145.

24. Romano S, Nezhadfar P, Shamsaei N, Sei M, Beretta S. High cycle fatigue behavior and life prediction for additively manufactured 17-4PH stainless steel: effect of sub-surface porosity and surface roughness. *Theor Appl Fract Mech*. 2020;106:102477.

25. Solberg K, Berto F. A diagram for capturing and predicting failure locations in notch geometries produced by additive manufacturing. *Int J Fatigue*. 2020a;134:105428.

26. Murakami Y. *Chapter 5 - effect of hardness HV on fatigue limits of materials containing defects, and fatigue limit prediction equations*, Metal Fatigue. Oxford: Elsevier Science Ltd; 2002. pp. 57-74.

27. ASTM F3055-14a. Standard Specification for Additive Manufacturing Nickel Alloy (UNS N07718) with Powder Bed Fusion. ASTM International, West Conshohocken, PA, 2014. https://www.astm.org

28. Zhang D, Niu W, Cao X, Liu Z. Effect of standard heat treatment on the microstructure and mechanical properties of selective laser melting manufactured Inconel 718 superalloy. *Mater Sci Eng A*. 2015;644:32-40.

29. Barba D, Alabort C, Tang Y, Viscasillas M, Reed R, Alabort E. On the size and orientation effect in additive manufactured Ti-6Al-4V. *Mater Des*. 2020;186:108235.

30. Solberg K, Berto F. The effect of defects and notches in quasi-static and fatigue loading of Inconel 718 specimens produced by selective laser melting. *Int J Fatigue*. 2020b;137:105637.

31. Yamashita Y, Murakami T, Mihara R, Okada M, Murakami Y. Defect analysis and fatigue design basis for Ni-based superalloy 718 manufactured by selective laser melting. *Int J Fatigue*. 2018;117:485-495.

32. Günther J, Krewerth D, Lippmann T, et al. Fatigue life of additively manufactured Ti6Al4V in the very high cycle fatigue regime. *Int J Fatigue*. 2017;94:236-245.

33. Solberg K, Guan S, Razavi SMJ, Welo T, Chan KC, Berto F. Fatigue of additively manufactured 316L stainless steel: the influence of porosity and surface roughness. *Fatigue Fract Eng Mater Struct*. 2019;42:2043-2052.

34. Dowling NE. *Mechanical behavior of materials*. 4th edition, Pearson; 2013.

35. Smith K, Topper T, Watson P. A stress-strain function for the fatigue of metals (stress-strain function for metal fatigue including mean stress effect). *J Mater*. 1970;5:767-778.

36. Murakami Y. Chapter 2 - stress concentration. *In: Metal Fatigue*: Elsevier Science Ltd, Oxford; 2002:11-24.

37. Taylor D. Geometrical effects in fatigue: a unifying theoretical model. *Int J Fatigue*. 1999;21(5):413-420.

38. Neuber H. Kerbspannungslehre. Springer-Verlag; 1958.

39. Neuber H. Uber die berucksichtigung der spannungskonzentration bei festigkeitsberechnungen. *Konstruktion*. 1968;20(7):245-251.

40. Susmel L. The theory of critical distances: a review of its applications in fatigue. *Eng Fract Mech*. 2018;75(7):1706-1724.

41. Louks R, Susmel L. The linear-elastic theory of critical distances to estimate high-cycle fatigue strength of notched metallic materials at elevated temperatures. *Fatigue Fract Eng Mater Struct*. 2014;38(6):629-640.

42. Greene GA. Greene GA, Finfrock CC. OXIDATION OF INCONEL 718 IN AIR AT TEMPER ATURES FROM 973 K TO 1620 K. Energy Sciences and Technology Department, Brookhaven National Laboratory; 2000. https://www.osti.gov/servlets/purl/777719

43. Kawagoishi N, Chen Q, Nisitani H. Fatigue strength of Inconel 718 at elevated temperatures. *Fatigue Fract Eng Mater Struct*. 2001;23(3):209-216.

44. Chen Q, Kawagoishi N, Nisitani H. Evaluation of notched fatigue strength at elevated temperature by linear notch mechanics. *Int J Fatigue*. 1999;21(9):925-931.

45. Nezhadfar P, Johnson AS, Shamsaei N. Fatigue behavior and microstructural evolution of additively manufactured Inconel 718 under cyclic loading at elevated temperature. *Int J Fatigue*. 2020;136:105598.

46. Prakash DGL, Walsh MJ, Maclachlan D, Korsunsky A. Crack growth micro-mechanisms in the IN718 alloy under the combined influence of fatigue, creep and oxidation. *Int J Fatigue*. 2009;31(11):1966-1977.

47. Zheng D, Rosenberger A, Ghonem H. Influence of prestraining on high temperature, low frequency fatigue crack growth in superalloys. *Mater Sci Eng A*. 1993;161(1):13-21.

48. Li Z, Luo AA, Wang Q, et al. Fatigue properties of cast magnesium wheels. *Metall and Mat Trans A*. 2016;47:4239-4257.

49. Connolley T, Starink MJ, Reed PAS. Effect of oxidation on high temperature fatigue crack initiation and short crack growth in Inconel 718. In: Proceedings of the 9th International Symposium on Superalloys The Minerals, Metals & Materials Society (TMS); 2000:435-444.